

# Modeled vortex dynamics on a Bose-Einstein condensate in a rotating lattice

P. Capuzzi<sup>1,2</sup> and D. M. Jezek<sup>2</sup>

<sup>1</sup>*Universidad de Buenos Aires, Facultad de Ciencias Exactas y Naturales,  
Departamento de Física. Buenos Aires, Argentina.*

<sup>2</sup>*CONICET - Universidad de Buenos Aires, Instituto de Física de Buenos Aires (IFIBA). Buenos Aires, Argentina.*

(Dated: March 24, 2025)

We study the dynamics of vortices in a Bose-Einstein condensate within a rotating four-site lattice which can be effectively described by a multimode model. Such a vortex dynamics develops along the low-density paths that separate the sites, and it is ruled by the phase differences between them. Hence, by appropriately selecting the initial conditions for on-site populations and phase differences, one can access distinct types of evolutions. We show that, by choosing equal populations in alternate sites, one can construct two-mode model Hamiltonians which allows us to model a large variety of associated vortex orbits. In particular, one can select the type of trajectory of the vortex and predict the creation and annihilation of vortex-antivortex pairs near the trap center. Estimates for the periods of closed vortex orbits and for the times that the vortices spend inside the lattice when dealing with open orbits, are obtained in terms of the two-mode models parameters and the rotation frequency only. We believe that the present study establishes a suitable platform to engineer different vortex dynamics.

## I. INTRODUCTION

The study of quantized vortices has been established as a central topic in the research on liquid Helium for several decades, since they represent a clear hallmark of superfluidity [1]. Such an interest has been latterly transferred to both experimental and theoretical works in cold atom systems, and in particular in Bose Einstein condensates (BECs)[2], in which the study of different phenomena involving vortices has constituted a very active area of research [3].

From the experimental point of view, such studies started with the first successful creation and observation of a vortex in 1999 [4]. This was followed by the measurement of the precession frequency of a vortex moving around the axis of a harmonic trapping potential [5]. Almost simultaneously, experiments on producing arrays of many vortices were carried out with rotating harmonic traps [6–8] and then, quadratic plus quartic potentials were employed to reach higher frequencies [9, 10]. Later on, experiments dealing with quantized circulation have also included toroidal trapping potentials [11–13]. Finally, in rotating optical lattices, different configurations of vortices were observed in triangular and square lattices by Tung *et al.* [14]. In particular, for sufficiently large rotation intensity, they reported a structural crossover to a vortex lattice. In addition, for a square lattice, the number of nucleated vortices as a function of the rotation frequency has been analyzed in Ref. [15].

Theoretical studies involving vortices also include different types of confining potentials and atomic species. Stationary configurations of arrays of vortices have been studied in rotating quadratic plus quartic potentials [16, 17] and in a nonrotating one [18]. The theoretical study of vortex dynamics in inhomogeneous nonrotating systems has constituted a challenging task due to the diverse density profiles produced in the different types of trapping potentials. The first studies were devoted to the

simpler case where the traps have an axial symmetry, and hence a single vortex precedes around such a symmetry axis. More recently, in more general inhomogeneous media, the vortex velocity has been derived in terms of the local density and its derivatives [18–22]. When several vortices are present, the velocity of a vortex is also affected by the velocity field generated by the rest of the vortices. Such an effect has been considered in a number of studies involving a few corotating vortices [23], vortices in rotating BECs that describe chaotic dynamics [24], the dynamics of vortex dipoles [25] observed in Ref. [26], quantum turbulence [27], interacting vortex lines in elongated BECs [28], doubly quantized vortices [29], and three-vortex configurations [30].

When the density itself varies as a function of time, the vortex dynamics becomes still much more difficult to describe. In the last years, in double-well systems, the passage of vortices along the junctions has been related to phase slips [31], and also the movement of vortices has been observed in solitonic systems [32, 33]. However, in the first case such a vortex passage has been difficult to trace because it occurs during much shorter timescales than the dynamics of the involved macroscopic variables, and also because vortex-antivortex pairs were generated or annihilated spontaneously during the evolution. In contrast, in the second case, the vortex dynamics is directly associated with the soliton velocity, since they move together, except around the collision of solitons where a more complicated vortex dynamics has been encountered.

In rotating systems, a very accurate multiple-mode (MM) model has been developed to study the dynamics of condensates within lattices which forms a system of weakly linked condensates (WLCs)[34]. In such a work, it has been shown that depending on the geometry of the condensates, different velocity profiles are imprinted on the localized on-site functions (LFs). In particular, for an on-site axial symmetry around the same direction of the

rotation axis, the corresponding LF exhibits a homogeneous velocity field. For WLCs in such conditions, it has been shown that the position of vortices along the low-density paths between sites can be analytically estimated [35]. The expression for such a position only involves the phase difference between sites, instead of the density gradients that appear in nonrotating systems. From such an expression, the number of nucleated vortices when ramping up linearly the rotation frequency, as done in the experiment of Ref. [15], has been calculated and shown to be in excellent agreement with Gross-Pitaevskii (GP) simulations. In the last year, a renewed interest in vortex dynamics in rotating condensates has arisen due to the possible relation to vortex dynamics in stars [36, 37]. We believe the position of vortices in such systems could be determined using an analogous expression, as a result of the distribution of particles inside the stars.

The aim of this work is to show that the vortex dynamics is determined only by the time-dependent phase differences between sites. Then, one can generate distinct patterns of vortices and make them describe predetermined types of orbits by appropriately choosing the initial populations and phase differences between sites of the rotating lattice. By constructing two-mode (TM) model Hamiltonians, we will demonstrate the diverse types of vortex dynamics that can be engineered for distinct values of the rotation frequency. The time evolution of the vortices shares the same period as those of Josephson or self-trapping oscillations in the TM model, thereby facilitating the tracking of the vortex trajectories.

The paper is organized as follows. In Sec. II we describe the theoretical background, which includes a summary of the method for obtaining the LFs, the description of the trapping potential, a brief analysis of the phase expressions for the on-site LFs obtained in Ref. [34]. We also analyze the formula for obtaining the vortex positions when the phase differences and populations evolve in time [35]. In Sec. III, we construct two Hamiltonians to obtain the different types of vortex patterns. We first describe some characteristics of the hopping parameter entering the Hamiltonians that determines the equations of motion, and then analyze the corresponding phase-space diagrams. In Sec. IV, we show a variety of vortex dynamics which includes closed and open orbits for both Hamiltonians. In most cases, estimates of characteristic times are presented. In Sec. V, we present our conclusions and the Appendix is devoted to exhibit the MM model equations of motion. There, we also derive a relation between the hopping parameter and energy differences of stationary states and discuss other useful parameters.

## II. THEORETICAL FRAMEWORK

### A. On-site localized functions and multimode model

We first review the construction of the MM model, which is then used to describe the vortex dynamics in terms of the populations and phase differences between the sites. An essential requirement for such a purpose consists in extracting accurate LFs. In previous works, it has been described the method for obtaining these localized states  $w_k(\mathbf{r})$  in either nonrotating [38, 39] or rotating [34, 35] ring-shaped lattices with  $N_s$  sites. Such LFs are given in terms of stationary states  $\psi_n(\mathbf{r}, \Omega)$ , which in turn are obtained by solving the Gross-Pitaevskii (GP) equation,

$$\left[ \hat{H}_0 + g N |\psi_n(\mathbf{r}, \Omega)|^2 - \Omega \cdot \hat{L} \right] \psi_n(\mathbf{r}, \Omega) = \mu_n \psi_n(\mathbf{r}, \Omega), \quad (1)$$

where  $n$  is restricted to  $-[(N_s - 1)/2] \leq n \leq [N_s/2]$  [34, 35]. The operator  $\hat{H}_0$  reads  $\hat{H}_0 = -\frac{\hbar^2}{2m} \nabla^2 + V_t(\mathbf{r})$ , where  $V_t(\mathbf{r})$  is the trapping potential,  $g$  is the 3D Rubidium coupling constant, and  $\Omega = \Omega \hat{z}$  is the applied rotation around the  $z$ -axis.

From such  $N_s$  orthonormal stationary states, the on-site LFs are obtained through the basis transformation [34, 35],

$$w_k(\mathbf{r}, \Omega) = \frac{1}{\sqrt{N_s}} \sum_n \psi_n(\mathbf{r}, \Omega) e^{-in\theta_k}, \quad (2)$$

where the index  $k$  labels the corresponding site, with  $-[(N_s - 1)/2] \leq k \leq [N_s/2]$  and  $\theta_k = 2\pi k/N_s$ .

Then, the MM model order parameter can be written using the orthonormal LFs as,

$$\psi_{\text{MM}}(\mathbf{r}, t) = \sum_k b_k(t) w_k(\mathbf{r}, \Omega), \quad (3)$$

where  $b_k(t) = \sqrt{n_k(t)} e^{i\phi_k(t)}$ , and  $N_k = n_k N$  is the occupation number. We note that the global phase  $\phi_k(t)$  does not represent the total phase in the  $k$ -site, but it takes into account only its time dependence, while the spatial profile of the phase, produced by the rotation, is carried out by the complex LFs,  $w_k(\mathbf{r}, \Omega)$ .

For obtaining the dynamics, we will use the time-dependent GP equation in the rotating frame, which reads

$$\left[ \hat{H}_0 + g N |\psi(\mathbf{r}, t)|^2 - \Omega \hat{L}_z \right] \psi(\mathbf{r}, t) = i\hbar \frac{\partial \psi(\mathbf{r}, t)}{\partial t}. \quad (4)$$

Equation (4) will be used to calculate the exact order parameter  $\Psi_{\text{GP}}(\mathbf{r}, t)$  and also serves for deriving the MM model equations of motion and its parameters [34]. For completeness, we include such a MM model approach in the Appendix.

We finally note that, by inverting the basis transformation in Eq. (2), the stationary states in terms of the

LFs acquire the form,

$$\psi_n(\mathbf{r}) = \frac{1}{\sqrt{N_s}} \sum_k w_k(\mathbf{r}) e^{ink2\pi/N_s}. \quad (5)$$

As we are interested in a four-site system, the subscript verifies  $n \in \{-1; 0; 1; 2\}$ . The stationary states have energies  $E_n$  that change their relative values when increasing the rotation frequency. In addition, the difference between energies with even (odd)  $n$  labels defines the real (imaginary) part of a hopping parameter (see Appendix). Each Hamiltonian will involve only the real or imaginary part of such parameter, and hence their signs will define the stationary points of the phase-space diagram. For both Hamiltonians, such stationary points will correspond to different stationary states given by Eq. (5).

### B. The trapping potential

In what follows, we will restrict our study to a four-well ring-shaped trapping potential given by,

$$V_t(\mathbf{r}) = \frac{1}{2}m [\omega_r^2 r^2 + \omega_z^2 z^2] + V_b [\cos^2(\pi x/q_0) + \cos^2(\pi y/q_0)], \quad (6)$$

where  $r^2 = x^2 + y^2$  and  $m$  is the atom mass. The harmonic frequencies are given by  $\omega_r = 2\pi \times 70$  Hz and  $\omega_z = 2\pi \times 90$  Hz, and the lattice parameter is  $q_0 = 5.1\mu\text{m} \simeq 3.939l_r$ , with  $l_r = \sqrt{\hbar/(m\omega_r)}$ . Hereafter, the time, energy, and length will be given in units of  $\omega_r^{-1}$ ,  $\hbar\omega_r$ , and  $l_r$ , respectively. The parameters of the trapping potential have been selected similar to those used in the experiment of Albiez *et al.* [40] in order to obtain a double-well system. With the purpose of forming four WLCs whose dynamics can be treated by the MM model, we further fix the barrier height and number of Rubidium atoms to  $V_b = 25\hbar\omega_r$  and  $N = 10^4$ , respectively. In Fig. 1 we show a scheme of the corresponding WLCs (left panel) and the location of the  $k$ -sites in the  $x - y$  plane (right panel).

### C. Phases on the on-site localized functions

For the trapping potential given by Eq. (6), it has been shown [34] that the imprinted velocity field within each localized function turns out to be homogeneous and it is given by  $\boldsymbol{\Omega} \times \mathbf{r}_{\text{cm}}^k$ , where  $\mathbf{r}_{\text{cm}}^k$  is the corresponding center of mass. Such a uniform velocity field is a consequence of the almost circular symmetry that acquires the on-site-localized density at the  $x - y$  plane for each  $z$  value. In particular, the LF for the  $k$ -site can be written as

$$w_k(\mathbf{r}, \Omega) = |w_k(\mathbf{r}, \Omega)| e^{i\frac{m}{\hbar}(\mathbf{r} - \mathbf{r}_{\text{cm}}^k) \cdot (\boldsymbol{\Omega} \times \mathbf{r}_{\text{cm}}^k)}, \quad (7)$$

where  $\mathbf{r}_{\text{cm}}^k$  is calculated using the localized density  $|w_k(\mathbf{r}, \Omega)|^2$ . As we will show, the linear dependence of the argument of  $w_k(\mathbf{r}, \Omega)$  on the coordinates turns out

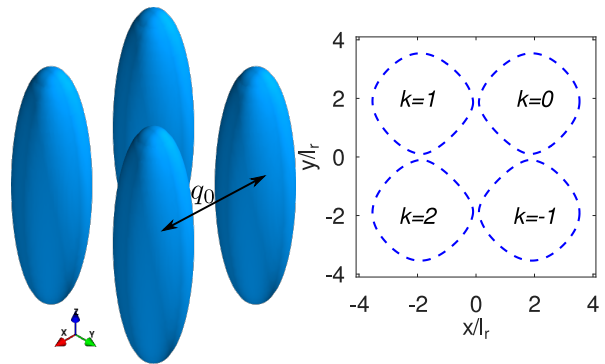


FIG. 1. A schematic illustration of the 4-site-lattice condensate is shown in the left panel, where  $q_0$  is the intersite distance. In the right panel, isodensity contours are depicted in blue dashed lines, at the  $z = 0$  plane, which correspond to the ground state for  $\Omega = 0$ . There, we also indicate the  $k$  value for each site.

to be helpful for determining the dynamics of vortices along the low-density paths of the lattice. We may further rewrite Eq. (7) in terms of the center-of-mass coordinates:  $\mathbf{r}_{\text{cm}}^k = (x_k, y_k, 0)$  as

$$w_k(\mathbf{r}, \Omega) = |w_k(\mathbf{r}, \Omega)| e^{i\frac{m}{\hbar}(yx_k - xy_k)\Omega}. \quad (8)$$

For the trapping potential here considered, the coordinates of the center of mass of the localized densities verify  $|x_k| = |y_k|$  and their absolute values may be approximated by  $q_0/2$ . In the next section, we will show that such a center of mass is in fact slightly shifted with respect to the value given by the lattice parameter, due to the presence of the harmonic confinement and the effect of the centrifugal force. Disregarding such effects, the LF at the  $k = 0$ -site can be approximated by

$$w_0(\mathbf{r}, \Omega) = |w_0(\mathbf{r}, \Omega)| e^{iA(-x+y)}, \quad (9)$$

where the factor in the phase reads  $A = \frac{m}{2\hbar} q_0 \Omega$ .

In the left panel of Fig. 2 we show the phase of  $w_0(x, y, 0)$ , where it may be seen it exhibits a linear coordinate-dependence behavior in accordance to Eq. (9) in the corresponding quadrant. It is important to note that the approximated expression given by Eq. (9) remains valid around the junctions [35] connecting neighboring sites. Then, as the MM model order parameter is a linear combination of LFs, we will use the analytic expressions of the phases along the low-density paths that separate the sites to determine the location of vortices.

### D. Analytical expressions for the vortex coordinates in terms of the multimode model variables

In this section, we briefly outline the method for obtaining the vortex positions developed for the study of nucleation of vortices in Ref. [35]. We will further show that for a rotating lattice and according to

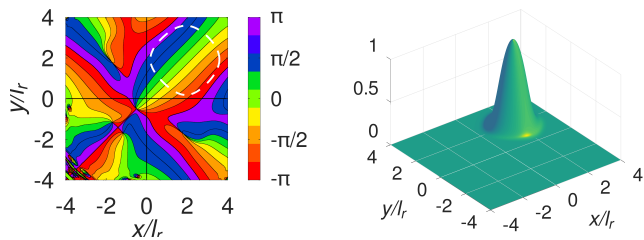


FIG. 2. The left panel shows the phase of  $w_0(x, y, 0)$  for  $\Omega/2\pi = 45$  Hz. The white dashed line indicates the isodensity contour of such a LF, with a value of  $10^{-3}$  of the density maximum  $\rho_{\max}$ . The color scale corresponds to  $\arg(w_0(\mathbf{r}))$ . In the right panel, we depict the renormalized density  $|w_0(x, y, 0)|^2/\rho_{\max}$ .

Eq. (3) the evolution of  $n_k(t)$  and  $\phi_k(t)$  determines the vortex dynamics. The condition for the presence of a vortex line with coordinates  $(X_v(t), Y_v(t), z)$  leads to a zero value in the time-dependent wavefunction, i.e.,  $\psi_{\text{MM}}(X_v(t), Y_v(t), z, t) = 0$ . Considering only the two neighboring LFs with  $k = 0$  and  $k = 1$ , and approximating their phases with the expressions of Eq. (8), one obtains the condition for the vortex coordinates along the low-density path  $x \simeq 0$  for  $y > 0$

$$\sqrt{n_0}e^{i\phi_0}|w_0|e^{iA(-X_v+Y_v)} + \sqrt{n_1}e^{i\phi_1}|w_1|e^{-iA(X_v+Y_v)} = 0. \quad (10)$$

Hence, defining  $\varphi_1 = \phi_1 - \phi_0$ , it leads to

$$e^{i(2AY_v - \varphi_1)}\sqrt{n_0}|w_0| + \sqrt{n_1}|w_1| = 0. \quad (11)$$

Therefore, from the imaginary part of the above equation we find the following condition

$$\sin(2AY_v(t) - \varphi_1(t)) = 0, \quad (12)$$

which implies that  $2AY_v(t) - \varphi_1(t) = k'\pi$ , whereas the real part of Eq. (11) restricts  $k' = 2l_y + 1$ . Hence, the vortex coordinate  $Y_v(t)$  evolves ruled by the time-dependent phase difference between the involved sites, following the law

$$Y_v^{(1)}(t) = \left( \frac{\varphi_1(t)}{\pi} + 2l_y + 1 \right) \frac{\pi\hbar}{mq_0\Omega}, \quad (13)$$

where  $l_y$  is an integer number. Hereafter, the superscript  $(k)$  on the coordinates will denote the low-density path between the sites labeled by  $k-1$  and  $k$ . We further note that, we will consider  $-\pi \leq \varphi_1(t) \leq \pi$ , which implies  $l_y \geq 0$ . Then, every time  $\varphi_1(t)$  crosses  $\pi$  the value of  $l_y$  should be increased by one unit. Such transitions occur at values of  $Y_v$  multiples of  $2\pi\hbar/(mq_0\Omega)$ . Hence, in the present study and for rotation frequencies larger than  $\Omega/2\pi \simeq 28$  Hz, two values  $l_y = 0, 1$  are needed for describing the whole vortex dynamics.

Additionally, from the real part of Eq. (11) one can infer that  $X_v^{(1)}(t)$  should oscillate following the  $n_k(t)$  evolution. Indeed, Eq.(11) leads to  $\frac{\sqrt{n_0(t)}|w_0(X_v, Y_v, Z_v)|}{\sqrt{n_1(t)}|w_1(X_v, Y_v, Z_v)|} = 1$ ,

which gives rise to a very small  $X_v^{(1)}$  oscillation amplitude around zero.

We may straightforwardly generalize the expression of the vortex coordinate given by Eq. (13) to the rest of the junctions by taking into account that the involved variable  $\varphi_k(t)$  may, in general, take a different value and thus the vortices in other junctions exhibit distinct dynamics. We may further note that for low  $\Omega$  values, the expression for the vortex coordinates can throw values  $Y_v \gg q_0$  and hence it can happen that at some times one does not observe any vortex inside the lattice. However, it does not exist a critical nucleation frequency, given that depending on the values of  $\varphi_k$  a vortex can appear when the phase difference acquires a value near  $\pm\pi$ .

### III. SYMMETRIC INITIAL CONDITIONS: REDUCTION TO TWO MODE MODEL SYSTEMS

In this section, we analyze the phase-space diagrams corresponding to TM model Hamiltonians obtained by considering that the initial populations and phase differences alternate their values when moving around the ring in the counterclockwise direction. In particular, we restrict to  $n_k(0) = n_{k+2}(0)$  and  $\varphi_k(0) = \varphi_{k+2}(0)$ . By introducing these conditions into the MM equations of motion given by Eqs. (A.1) and (A.2), only a single hopping parameter  $K$  and an effective interaction parameter  $U_{\text{eff}}$  are involved (see Appendix). Furthermore, whether  $\varphi_k(0) + \varphi_{k+1}(0) = 0$  or  $\varphi_k(0) + \varphi_{k+1}(0) = \pi$ , the real part or the imaginary part of  $K$  is retained in such equations, respectively. By defining the conjugated coordinates  $Z = 2(n_0 - n_1) = 2\Delta N/N$  and  $\varphi = \varphi_1$ , one can easily construct both TM model Hamiltonians. We will first discuss the dependence of such TM model parameters on the rotation frequency.

#### A. Parameters involved in the model

We note that in the static case, the effective on-site interaction energy is given by a positive real number,  $U_{\text{eff}} = 2.269 \times 10^{-3}\hbar\omega_r$ , which remains almost constant for increasing rotation frequencies (see [38]). On the other hand, for nonzero  $\Omega$  values the hopping parameter  $K$  becomes a complex number with a decreasing absolute value as a function of  $\Omega$ . For this trapping potential, it has been shown that the LFs acquire a linear phase which gives rise to an almost homogeneous velocity field on each site when the system is subject to rotation [34]. Such a particular phase profile determines the phase  $\Theta$  of the hopping parameter  $K$  (see Appendix). In Fig. 3, the real and imaginary part of  $K$  are depicted as function of  $\Omega$ , which will define the distinct types of vortex dynamics of the present study.

Taking into account that  $K = |K|e^{i\Theta}$ , with  $\Theta = -m\Omega r_{\text{cm}}^2 \sin(2\pi/N_s)/\hbar$  (see Appendix), for our four-site

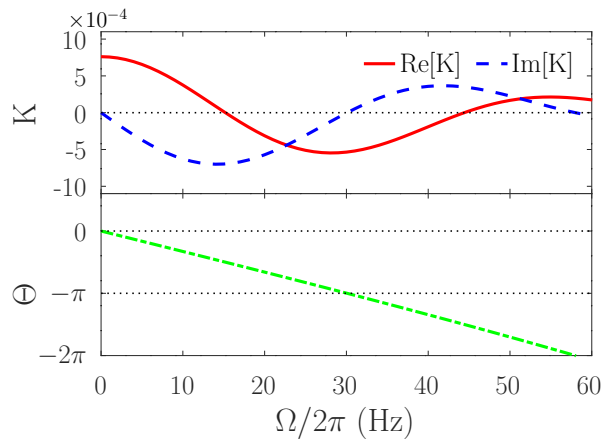


FIG. 3. Top panel: Real part (red solid line) and imaginary part (blue dashed line) of the hopping parameter  $K$  as function of the rotation frequency. Bottom panel: the argument of  $K$  as a function of the frequency is depicted as a green dashed-dotted line.

lattice one can roughly approximate the absolute values of the center-of-mass coordinates in terms of the intersite distance  $|x_k| = |y_k| \simeq q_0/2$ , yielding

$$\Theta \simeq -\Omega q_0^2 l_r^{-2} / (2\omega_r). \quad (14)$$

However, in the previous formula we have disregarded the effect of the harmonic trap, which lowers  $r_{\text{cm}}^2$ , and of the centrifugal force, which slightly increases the  $r_{\text{cm}}^2$  of the on-site localized density with  $\Omega$ . Therefore, a better estimate of  $r_{\text{cm}}^2$  can be obtained by considering that the net force applied to the on-site center-of-mass equals zero. Approximating the lattice potential around its minima to second order in the coordinates, and equating the sum of the forces given by the harmonic trap, the lattice potential, and the centrifugal one, it yields

$$|x_k| = |y_k| \simeq \frac{V_b \pi^2 q_0}{q_0^2 m (\omega_r^2 - \Omega^2) + 2V_b \pi^2}. \quad (15)$$

In Fig. 4, it may be seen that the center-of-mass radius  $r_{\text{cm}}$  evaluated using LFs is, indeed, an increasing function of  $\Omega$ . Furthermore, when such a rotation frequency reaches the harmonic trap frequency  $\omega_r$ , all estimates verify  $r_{\text{cm}} = q_0/\sqrt{2}$ , given that the repulsion of the centrifugal force cancels the attraction of the harmonic trap. Moreover, we note that the approximate value obtained through Eq. (15) reproduces the exact result within a relative error less than 0.01.

The frequencies where either  $\Re(K)$  or  $\Im(K)$  vanish are crucial, since at such frequencies the phase-space diagrams undergo qualitative changes, as will be discussed in detail in the next section. In Fig. 5, it may be seen that  $\Theta$  as a function of  $\Omega$  slightly deviates from the linear approximation depicted as a red dashed line. In particular, using the linear approximation given by Eq. (14)

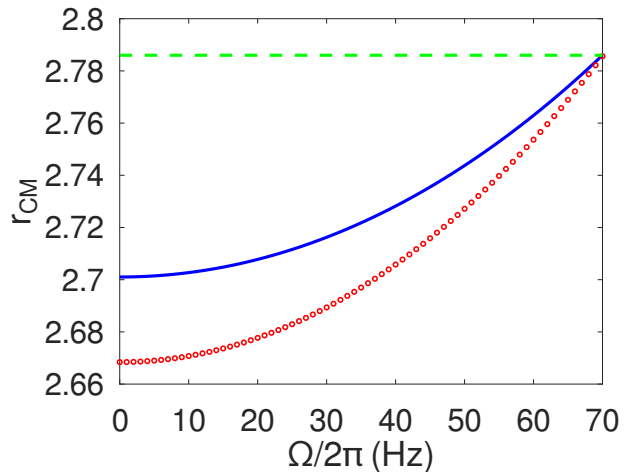


FIG. 4. Absolute value of the center-of-mass position  $r_{\text{cm}}$  as a function of the rotation frequency. The exact value obtained using the LFs is depicted with red hollow circles. The solid blue line is the estimate obtained from the approximation of Eq. (15). The rough value, given only in terms of the lattice-intersite distance, yields  $r_{\text{cm}} \simeq q_0/\sqrt{2} = 3.939 l_r/\sqrt{2} = 2.786 l_r$  and it is shown as the horizontal green dashed line.

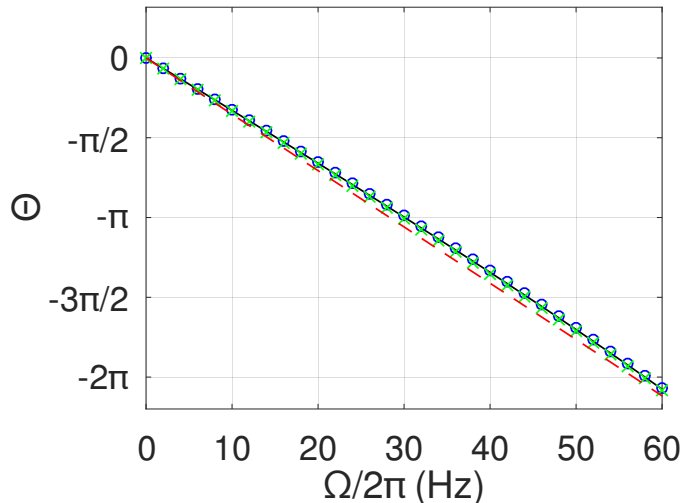


FIG. 5. Comparison between different estimates for the argument  $\Theta$  of the hopping parameter as a function of the rotation frequency. The solid black line represents the exact value of the argument of  $K$ . The better estimates are obtained from Eq. (A.8) with the  $r_{\text{cm}}$  evaluated by either GP simulations (blue hollow circles) or Eq. (15) (green crosses), whereas the less accurate value is given by Eq. (14) using  $q_0 = 3.939 l_r$  which is shown as a red dashed line.

for searching  $\Im(K) = 0$ , one obtains  $\Omega/2\pi \simeq 28.3$  Hz for  $\Theta = -\pi$ , whereas the exact expression yields  $\Omega/2\pi \simeq 30$  Hz. Then, if one wants to analytically obtain accurate critical rotation frequencies for the vanishing of  $\Re(K)$  and  $\Im(K)$ , one should take into account the effect of the forces acting on the center of mass of each site. From

such a better estimate, one can also obtain the vanishing  $\Re(K)$  values, which for  $\Theta = -\pi/2$  and  $\Theta = -3\pi/2$ , are attained around  $\Omega_0/2\pi \simeq 15\text{Hz}$  and  $\Omega_0/2\pi \simeq 45\text{ Hz}$ , respectively.

### B. Two-mode model Hamiltonians and phase-space diagrams

In this section, in order to analyze the phase-space diagram we first construct two Hamiltonians  $H_i(Z, \varphi)$  with  $i = 0, 1$ , making use of the equations of motion (A.1) and (A.2) restricted to particular initial conditions. Then, we define conjugate coordinates  $Z$  and  $\varphi$  such that the equations of motion reads,

$$\frac{d\varphi}{dt} = \frac{\partial H_i}{\partial Z} \quad (16)$$

and

$$\frac{dZ}{dt} = -\frac{\partial H_i}{\partial \varphi}. \quad (17)$$

Given that the critical points, minima, maxima, and saddles of the Hamiltonians organize the types of regimes inside the phase-space diagram, we analyze their positions when changing the rotation frequency.

#### 1. Two-mode model Hamiltonian that involves the real part of the hopping

We first consider the case  $\varphi_k(0) + \varphi_{k+1}(0) = 0$  in Eqs. (A.1) and (A.2). Given that such symmetry holds during all the evolution, it has been shown [41] that the equations of motion (A.1) and (A.2) reduce to that of a two-mode system with Hamiltonian  $H_0$  given by

$$H_0(Z, \varphi)/\gamma_0 = \frac{\Lambda_0}{2} Z^2 - \text{sign}(\Re(K)) \sqrt{1 - Z^2} \cos(\varphi), \quad (18)$$

for  $\Re(K) \neq 0$ ,  $\Lambda_0 = NU_{\text{eff}}/(4|\Re(K)|)$ ,  $\gamma_0 = 2|\Re(K)|/\hbar$ . And

$$H_0^{(c)} = \frac{NU_{\text{eff}}}{4\hbar} Z^2, \quad (19)$$

for  $\Re(K) = 0$ , which occurs at a critical value  $\Omega = \Omega_0$ .

In the latter case, the critical values in the range of the rotation frequencies studied (see Fig. 3) are  $\Omega_0^{(1)}/2\pi \simeq 15\text{ Hz}$  and  $\Omega_0^{(2)}/2\pi \simeq 45\text{ Hz}$ . For  $0 \leq \Omega < \Omega_0^{(1)}$  and  $\Omega_0^{(2)} < \Omega$  the phase-space diagrams exhibit a Hamiltonian minimum at  $Z = 0$  and  $\varphi = 0$ , around which, closed orbits are present. Such orbits are called plasma- or 0-modes. A saddle point located at  $Z = 0$  and  $\varphi = \pi$  defines the Hamiltonian value for the separatrix between the closed and open orbits. The open orbits exhibit a running phase difference typical of the self-trapping (ST) regime, which is characterized by an imbalance  $Z$  that never vanishes. For the lower frequency interval, the corresponding

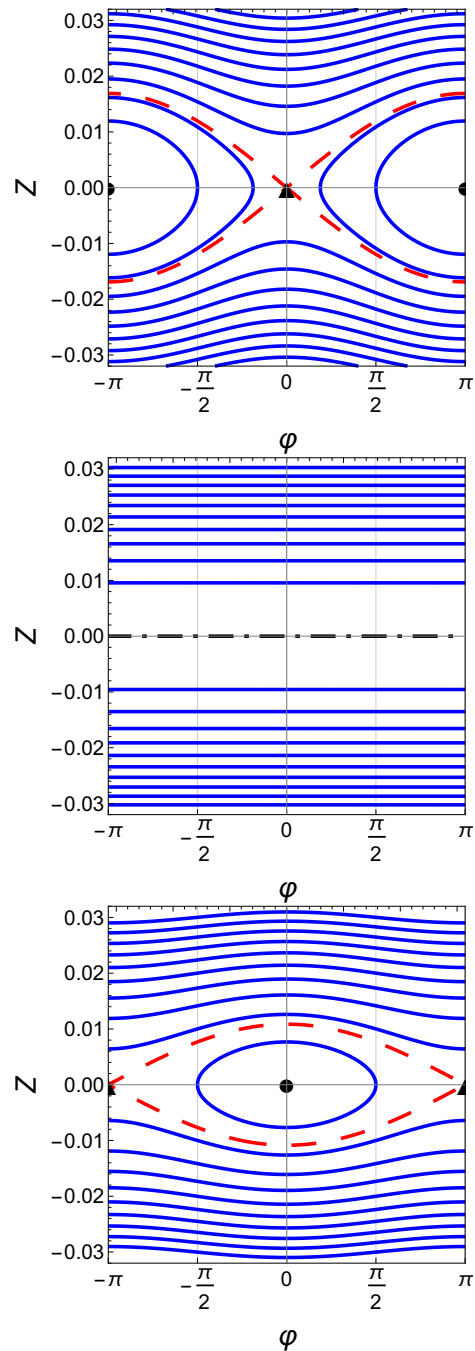


FIG. 6. Phase-space diagrams of  $H_0$  for  $\Omega/2\pi = 35\text{ Hz}$  (top panel), for the critical frequency  $\Omega_c/2\pi = 45\text{ Hz}$  (middle panel), and for  $\Omega/2\pi = 50\text{ Hz}$  (bottom panel). The TM orbits are depicted with solid blue lines and the separatrices between closed and open orbits with dashed red lines. The stationary points are indicated with a dot (minimum) and with a filled triangle which corresponds to a saddle point. The black dot-dashed line in the middle panel indicates a one dimensional variety of stationary points.

phase-space diagram has been studied previously in [41]. Here, we show the phase-space diagram for  $\Omega/2\pi = 50\text{ Hz}$  in the bottom panel of Fig. 6. In the rotation frequency

interval  $\Omega_0^{(1)} < \Omega < \Omega_0^{(2)}$ , the Hamiltonian minimum moves to  $Z = 0$  and  $\varphi = \pi$  around which closed orbits called  $\pi$ -modes are present, whereas  $Z = 0$  and  $\varphi = 0$  becomes the new saddle point (top panel of Fig. 6). For both plasma and  $\pi$  modes, the maximum difference of the particle numbers is  $\Delta N_c = N\sqrt{\Lambda_0 - 1}/\Lambda_0$ , which is attained at  $\varphi = 0$  and  $\varphi = \pi$ , respectively.

The MM states associated to the dynamics restricted to the symmetry that gives rise to  $H_0$  do not exhibit vortices at the center of the  $x-y$  plane, except for  $Z = 0$  and  $\phi = \pi$ . This can be verified using the expression of the order parameter with the four localized functions, which at  $x = y = 0$  yields

$$\psi_{\text{MM}} = 2|w_0(0, 0, z)| (\sqrt{n_0}e^{i\phi_0} + \sqrt{n_1}e^{i\phi_1}), \quad (20)$$

where we have used that  $|w_k(0, 0, z)| = |w_0(0, 0, z)|$ . From the previous expression, one can assure that

$$\psi_{\text{MM}} = 2|w_0(0, 0, z)| e^{i\phi_0} (\sqrt{n_0} + \sqrt{n_1}e^{i\varphi}) \neq 0, \quad (21)$$

except for  $\varphi = \pi$  and  $Z = 0$ , which is always a stationary point and hence it does not participate in any dynamics.

It is interesting to note that the stationary points of the phase-space diagrams at  $\varphi = 0$  (bottom panel of Fig. 6) and  $\varphi = \pi$  (top panel) correspond to the GP-stationary states  $\psi_0(\mathbf{r})$  and  $\psi_2(\mathbf{r})$ , respectively, as it can be seen from Eq. (5). Hence, the minimum is related to different  $n$  values depending on the selected range of the rotation frequency. Although the central, doubly quantized vortex at the  $z$ -axis does not survive in the surrounding region of the phase-space diagram, we will see that it is connected to a two-vortex dynamics around such an axis.

## 2. Two-mode model Hamiltonian that involves the imaginary part of the hopping

A different type of dynamics arises if we consider  $\varphi_k(0) + \varphi_{k+1}(0) = \pi$ . In such a case, the equations of motion (A.1) and (A.2) give rise to the following TM model Hamiltonian,

$$H_1/\gamma_1 = \frac{\Lambda_1}{2} Z^2 + \text{sign}(\Im(K))\sqrt{1 - Z^2} \sin(\varphi), \quad (22)$$

for  $\Im(K) \neq 0$ ,  $\Lambda_1 = NU_{\text{eff}}/(4|\Im(K)|)$ , and  $\gamma_1 = 2|\Im(K)|/\hbar$ .

In the particular case of  $\Im(K) = 0$ , one has the same expression for the critical Hamiltonian as that given by Eq. (19),

$$H_1^{(c)} = \frac{NU_{\text{eff}}}{4\hbar} Z^2. \quad (23)$$

The condition  $\Im(K) = 0$  is attained around  $\Omega_1/2\pi \simeq 30$  Hz. For  $0 \leq \Omega < \Omega_1$ , the phase-space diagram exhibits a Hamiltonian minimum at  $Z = 0$  and  $\varphi = \pi/2$ . Around such a point, the closed orbits, which can be viewed in the upper panel of Fig. 7, will be referred to

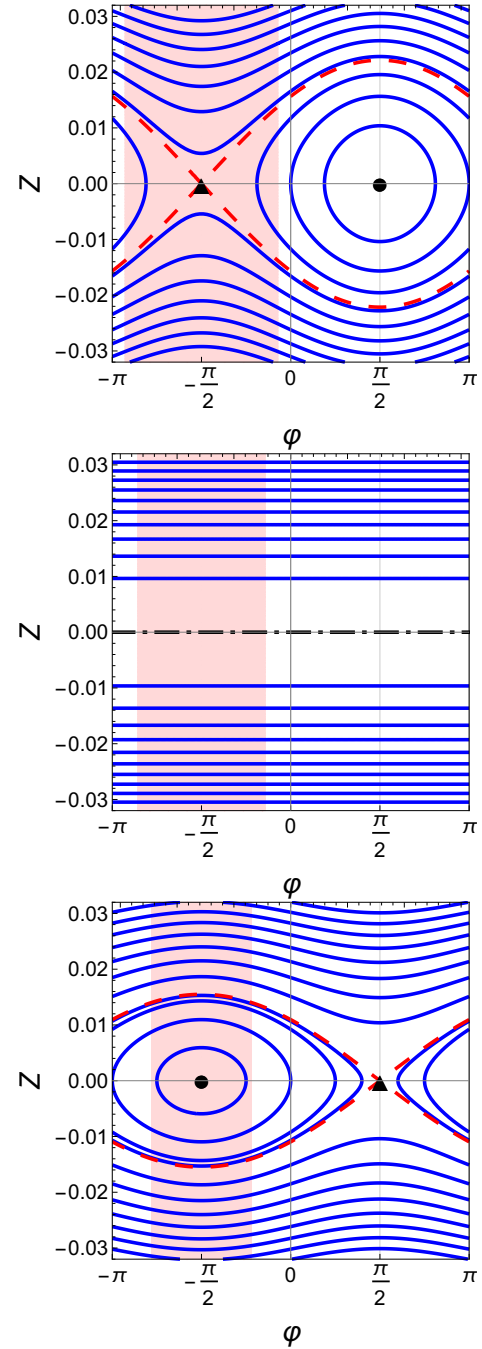


FIG. 7. Phase-space diagrams of  $H_1$  for  $\Omega/2\pi = 15$  Hz (top panel), for the critical frequency  $\Omega_c/2\pi = 30$  Hz (middle panel), and for  $\Omega/2\pi = 45$  Hz (bottom panel). The TM orbits are depicted with solid blue lines and the separatrices between closed and open orbits with red dashed lines. The stationary points are indicated with a dot (minimum) and with a filled triangle which corresponds to a saddle point. The black dot-dashed line in the middle panel indicates a one dimensional variety of stationary points. The pink-shaded areas indicate the regions with the presence of a central antivortex.

as  $\pi/2$ -modes. The saddle point located at  $Z = 0$  and  $\varphi = -\pi/2$  determines the Hamiltonian value that defines

the separatrix (depicted with red dashed lines) between the closed orbits and the open ones that belong to the ST regime. In the middle panel of Fig. 7, it may be viewed that  $Z$  remains constant. In particular, the black dot-dashed line at  $Z = 0$  represents a set of stationary points. For rotation frequencies  $\Omega_1 < \Omega$ , the Hamiltonian minimum turns out to be at  $Z = 0$  and  $\varphi = -\pi/2$ , see bottom panel of Fig. 7. Around such a point, closed orbits are present, which will be called  $-\pi/2$ -modes. The saddle point in this case is located at  $Z = 0$  and  $\varphi = \pi/2$ .

For both the  $\pi/2$ -mode and the  $-\pi/2$ -mode the maximum difference of the particle numbers is  $\Delta N_c = N\sqrt{\Lambda_1 - 1}/\Lambda_1$ , which is attained at  $\varphi = \pi/2$  and  $\varphi = -\pi/2$ , respectively. For larger imbalances, the ST dynamics develops.

The Hamiltonian  $H_1$  is related to systems with a permanent central vortex, and hence the velocity circulation around the lattice is nonzero for any rotation frequency. However, the central vortex can invert its charge during the dynamics. In particular, the phase-space diagrams become partitioned into regions with either a vortex or an antivortex. In the phase-space diagrams of Fig. 7, we show as pink-shaded areas the regions where an antivortex is present along the  $z$ -axis. Hence, when crossing the borders of such areas, creation or annihilation of vortex-antivortex pairs occurs to produce the change of the central vortex charge.

In order to prove the existence of such a central vortex, we can examine the MM model order parameter at the  $z$  axis using that  $|w_k(0, 0, z)| = |w_0(0, 0, z)|$ . There, it can be written as

$$\psi_{\text{MM}} = |w_0| \left( \sqrt{n_0} + \sqrt{n_1} e^{i\varphi} + \sqrt{n_0} e^{i\pi} + \sqrt{n_1} e^{i(\varphi+\pi)} \right), \quad (24)$$

which vanishes for all  $\varphi$  and  $Z$  values. Then, we conclude that a central vortex is always present for any time evolution, while the actual charge of such a vortex depends on the region of the phase-space diagram where the orbit passes through.

The stationary points of the phase-space diagrams for this Hamiltonian correspond to the GP-stationary states  $\psi_1(\mathbf{r})$  and  $\psi_{-1}(\mathbf{r})$ , for  $\varphi = \pi/2$  and  $\varphi = -\pi/2$ , respectively, as it can be shown by comparing  $\psi_{\text{MM}}$  of Eq. (3) with equal populations and the condition on the phases, with Eq. (5). The state with  $n = 1$  ( $n = -1$ ) corresponds to a central vortex (antivortex) state; hence, its corresponding coordinates lie within the non shaded (shaded) area of Fig. 7. It is interesting to note that the shaded areas become narrower when the rotation frequency increases, thus decreasing the probability of finding such central antivortices.

## IV. VORTEX DYNAMICS

### A. Vortex dynamics at the critical frequencies

We will analyze the dynamics related to the Hamiltonian  $H_0^{(c)}$  and  $H_1^{(c)}$  where either  $\Re(K) = 0$  or  $\Im(K) = 0$ , respectively. In both cases we have  $\dot{\varphi} = \frac{NU_{\text{eff}}}{2\hbar} Z$  and  $\dot{Z} = 0$ . Then, if  $\varphi(0) = 0$ ,

$$\varphi(t) = \frac{NU_{\text{eff}}}{2\hbar} Zt = \frac{\Delta NU_{\text{eff}} t}{\hbar}. \quad (25)$$

Hence, the time period  $\tau$  for the phase difference to increase  $2\pi$  yields

$$\tau = \frac{2\pi\hbar}{\Delta NU_{\text{eff}}}. \quad (26)$$

We note that, as  $\dot{\varphi}(t) \neq 0$  during all the evolution, the vortex trajectories do not exhibit turning points (cf. Eq. (13)).

Another relevant time interval is the time  $T_t$  that a vortex spends in traveling from the trap center to outside the lattice, which can be estimated by considering the lattice limits as  $|y| < q_0$ , and using,

$$Y_v^{(1)}(t) = \left( \frac{\Delta NU_{\text{eff}} t}{\hbar\pi} + 2l + 1 \right) \frac{\pi\hbar}{mq_0\Omega}, \quad (27)$$

which yields

$$T_t \simeq \frac{mq_0^2\Omega}{\Delta NU_{\text{eff}}}. \quad (28)$$

In contrast to  $\tau$ , this traveling time increases linearly with  $\Omega$ .

#### 1. Dynamics related to the real part of the hopping, with even number of vortices

Due to the symmetry of the system and the initial conditions, we can restrict the study of the vortex dynamics to that developed along two low-density paths. We focus on the paths identified by the coordinates superscript ( $k$ ) with  $k = 0$  and  $k = 1$ , which correspond to the positive semiaxes  $x$  and  $y$ , respectively. Then, for the Hamiltonian  $H_0^{(c)}$ , where  $\Re(K) = 0$ , using vanishing initial phase differences, such vortex coordinates acquire the form

$$Y_v^{(1)}(t) = \left( \frac{\Delta NU_{\text{eff}} t}{\hbar\pi} + 2l_y + 1 \right) \frac{\pi\hbar}{mq_0\Omega}, \quad (29)$$

at the junction (1), and

$$X_v^{(0)}(t) = \left( \frac{-\Delta NU_{\text{eff}} t}{\hbar\pi} + 2l_x + 1 \right) \frac{\pi\hbar}{mq_0\Omega}, \quad (30)$$

at the junction (0). Hence, taking into account the present symmetry for the dynamics along the other

low-density paths, one has  $X_v^{(2)}(t) = -X_v^{(0)}(t)$  and  $Y_v^{(-1)}(t) = -Y_v^{(1)}(t)$ . Then, if  $N_0 > N_1$  the vortices enter with constant velocity along the  $x$ -axis and depart from the system along the  $y$ -axis.

In Fig. 8 we show the vortex trajectories in the  $x - y$  plane, where the positions have been extracted from  $\psi_{\text{MM}}(\mathbf{r}, t)$  of Eq. (3) using the plaquette method of Ref. [42]. It is interesting to note that, although the incoming vortices approach the  $z$ -axis at the same time, they never form a doubly quantized vortex since the trajectories are well separated at the origin (see Fig. 8). For such a figure we have chosen a large imbalance  $\Delta N = 1000$  to amplify this behavior. In particular, it may be seen that the vortex coming from the positive  $x$  axis,  $X_v^{(0)}(t)$ , is slightly pushed to negative  $y$  values, and since the vortex then moves away along the  $y < 0$  junction, given by  $Y_v^{(-1)}(t)$ , it never touches the  $z$  axis. On the other hand, the incoming vortex from the negative  $x$  values  $X_v^{(2)}(t)$  moves away along the  $y > 0$  junction, yielding  $Y_v^{(1)}(t)$ . Such shifts from the axes are in accordance with the condition  $\sqrt{n_0(t)}|w_0(X_v, Y_v, Z_v)| = \sqrt{n_1(t)}|w_1(X_v, Y_v, Z_v)|$  derived from the real part of Eq. (11), given that  $n_0(t) > n_1(t)$ , it implies that the vortex is nearer the  $k = 1$ -site than the  $k = 0$  one.

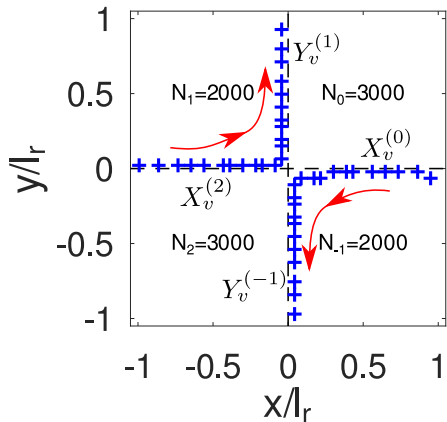


FIG. 8. Trajectories of two vortices near the trap center. The coordinates are extracted from  $\psi_{\text{MM}}(\mathbf{r}, t)$  using a plaquette method and are marked with blue plus signs. We use a large  $\Delta N = 1000$  value and a rotation frequency  $\Omega_c/2\pi = 15$  Hz. The arrows indicate the vortex velocity direction in each low-density path. Such density paths are indicated by the relevant coordinate with its superscript.

Hereafter, in this section we will work with  $\Delta N = 100$ , so that any shift from the axes becomes negligible. We note that, this imbalance yields a smaller time period, which allows us to better follow the dynamics.

The result for the vortex dynamics at two values of the critical frequency  $\Omega_c$  is depicted in Fig. 9, where the time

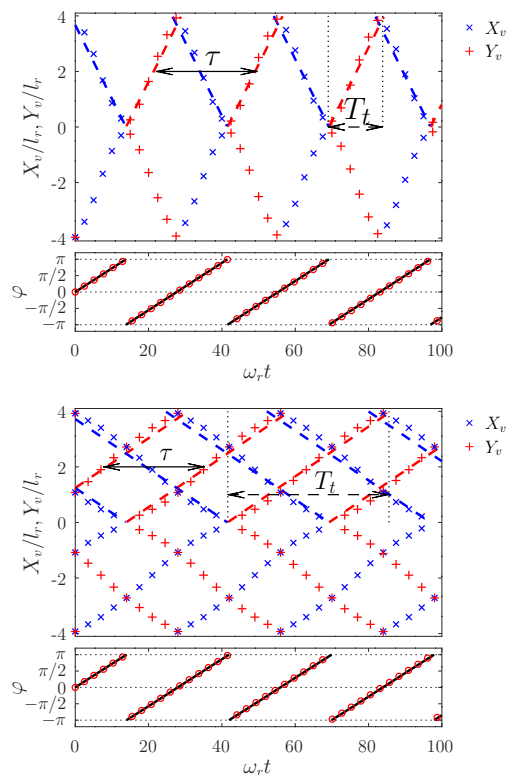


FIG. 9. Vortex coordinates as functions of time extracted from  $\psi_{\text{MM}}(\mathbf{r}, t)$  for  $\Omega_c/2\pi = 15$  Hz (top panel) and  $\Omega_c/2\pi = 45$  Hz (bottom panel) with  $\Delta N = 100$  and  $\varphi(0) = 0$ . The blue crosses and red plus signs of the positive values indicate the coordinates  $X_v^{(0)}(t)$  and  $Y_v^{(1)}(t)$ , respectively. The same symbols are utilized for the negative values which correspond to  $X_v^{(2)}(t)$  and  $Y_v^{(-1)}(t)$ . The dashed red and blue lines represent the predicted values from Eqs. (29) and (30), respectively. The horizontal lines indicate the period  $\tau = 27.6\omega_r^{-1}$  (solid) and the traveling times (dashed)  $T_t = 14.8\omega_r^{-1}$  (top)  $T_t = 43.9\omega_r^{-1}$  (bottom). Below each panel, the phase difference  $\varphi(t)$  is depicted using the MM model given by Eq. (25) as a solid black line and the GP values are shown as red circles. The GP phase difference is calculated from  $\Psi_{\text{GP}}(\mathbf{r}, t)$  as the difference of the phases between the centers of the corresponding sites.

evolution of the vortex positions  $X_v^{(0)}(t)$ ,  $Y_v^{(1)}(t)$ ,  $X_v^{(2)}(t)$ , and  $Y_v^{(-1)}(t)$ , along each semiaxis are shown as function of time for  $\Omega_c/2\pi = 15\text{Hz}$  (top panel), and  $\Omega_c/2\pi = 45\text{Hz}$  (bottom panel). The initial condition  $\varphi(0) = 0$  implies that the initial coordinate reads  $Y_v^{(1)}(0) \simeq 3.7l_r$  and  $Y_v^{(-1)}(0) \simeq 1.2l_r$ , for the top and bottom panels, respectively. The population imbalance is  $\Delta N = 100$  which yields a time period, given by Eq. (26),  $\tau = 27.6\omega_r^{-1}$ . Such a period can be viewed in the vortex dynamics as the time interval between two successive vortices pass by the same point of the  $x - y$  plane. In Fig. 9 it may be seen that the theoretical value is in good accordance with the evolution in both panels. The traveling times given by Eq. (28) for the top and bottom panels yield

$T_t = 14.8\omega_r^{-1}$  and  $T_t = 43.9\omega_r^{-1}$ , respectively, which implies that the vortices inside the lattice move slower when the rotation frequency is increased. Below each panel one can observe a perfect accordance of the phase difference  $\varphi(t)$  obtained by the MM model and its corresponding GP simulation. Such type of open orbits are obtained also in the self-trapping regime, where a running phase is developed. However, in such a case the vortex trajectories exhibit a little oscillation in the perpendicular direction due to the imbalance oscillation.

2. *Dynamics that involves the imaginary part of the hopping, with odd number of vortices*

The dynamics related to the Hamiltonian  $H_1^{(c)}$ , where  $\Im(K) = 0$ , have substantial differences with the previous one. First, we recall that a central vortex or an antivortex is always present along the  $z$ -axis. If the initial phase difference at the junction (1) is zero, the junction (0) should exhibit initially a  $\pi$  phase difference, since  $\varphi_k + \varphi_{k+1} = \pi$  for  $H_1$ . Therefore, the motion of the vortices are described by,

$$Y_v^{(1)}(t) = \left( \frac{\Delta N U_{\text{eff}} t}{\hbar \pi} + 2l_y + 1 \right) \frac{\pi \hbar}{mq_0 \Omega}, \quad (31)$$

at the low-density path (1), and

$$X_v^{(0)}(t) = \left( -\frac{\Delta N U_{\text{eff}} t}{\hbar \pi} + 2l_x \right) \frac{\pi \hbar}{mq_0 \Omega}, \quad (32)$$

at the low-density path (0). Along the negative semiaxes one has  $X_v^{(2)}(t) = -X_v^{(0)}(t)$  and  $Y_v^{(-1)}(t) = -Y_v^{(1)}(t)$ . From Eqs. (31) and (32) one can see that the coordinates vanish at different times, implying that a vortex departs from the trap center along the  $y$ -axis before another enters along the  $x$ -axis. Then, in the whole lattice, when two vortices leave the trap center along the  $y$ -axis, the central vortex becomes an antivortex until the other two vortices reach the central zone coming from the  $x$ -axis, as shown in Fig. 10. Such a process necessarily involves the creation and then the annihilation of a vortex-antivortex pair to locally conserve the velocity-field circulation.

**B. Vortex dynamics related to the closed orbits in the phase-space diagrams**

The stationary points on the phase-space diagram also define stationary vortex states if the corresponding vortex coordinates are inside the lattice edge, which is the case for high enough frequencies. In particular, the minima of the Hamiltonian that are associated with closed orbits in the phase-space diagram give rise to closed orbits around the stationary vortex. For such vortices, the small-oscillation period is the same as that of the Hamiltonian orbits. Therefore, the time period near such min-

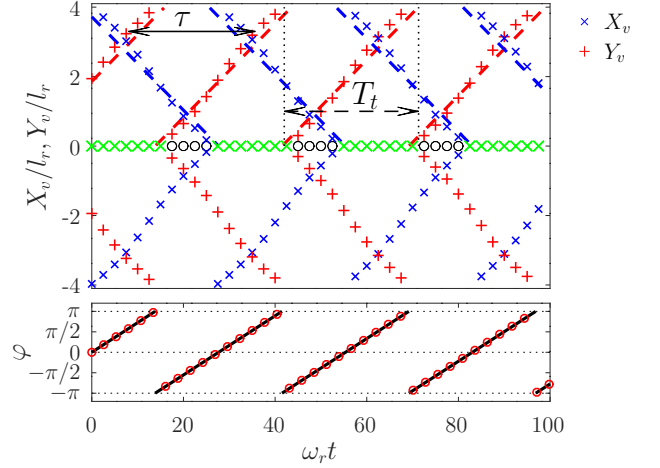


FIG. 10. Vortex coordinates as functions of time extracted from the  $\psi_{\text{MM}}(\mathbf{r}, t)$  using the plaquette method are shown in the top panel. The blue crosses and red plus signs of the positive coordinate values indicate  $X_v^{(0)}(t)$  and  $Y_v^{(1)}(t)$ , respectively, whereas the same symbols are utilized for the negative values which correspond to  $X_v^{(2)}(t)$  and  $Y_v^{(-1)}(t)$ . The green crosses and the black circles indicate the central vortices and antivortices, respectively. The dashed red and blue lines represent the predicted values from Eqs. (31) and (32), respectively. The horizontal lines indicate the period  $\tau = 27.6\omega_r^{-1}$  (solid) and the traveling time  $T_t = 29.3\omega_r^{-1}$  (dashed). The initial conditions correspond to  $\Delta N = 100$  and  $\varphi = 0$ , for  $\Omega_c/2\pi = 30$  Hz. In the bottom panel the corresponding phase difference  $\varphi(t)$  is shown as a function of time. The results extracted from GP simulations and the MM model are depicted with red circles and a solid black line, respectively.

ima can be evaluated using the small oscillation approximation [43], which yields

$$\tau_{\text{SO}} = \frac{\pi \hbar}{\mathcal{K}_i \sqrt{\Lambda_i + 1}}, \quad (33)$$

for  $i = 0; 1$  with  $\mathcal{K}_0 = |\Re(K)|$  and  $\mathcal{K}_1 = |\Im(K)|$ .

1. *Closed orbits involving  $\pi$  and plasma modes*

For  $\pi$  and plasma modes one has the following vortex coordinates,

$$Y_v^{(1)}(t) = \left( \frac{\varphi(t)}{\pi} + 2l_y + 1 \right) \frac{\pi \hbar}{mq_0 \Omega}, \quad (34)$$

$$X_v^{(0)}(t) = \left( -\frac{\varphi(t)}{\pi} + 2l_x + 1 \right) \frac{\pi \hbar}{mq_0 \Omega}, \quad (35)$$

In the case  $\Re(K) < 0$ ,  $\pi$ -modes appear in the phase-space diagram. Such orbits give rise to closed orbits of vortices. Each turning point of  $\varphi$  is related to a turning point of the vortex coordinate along the low-density

path. The other coordinate in the transversal direction moves from one site border to the neighboring one due to the sign change of  $Z$ . In Fig. 11 we show  $Y_v^{(k)}(t)$  for  $\Delta N = 60$  and  $\Omega/2\pi = 35\text{Hz}$ , corresponding to a negative value  $\Re(K) = -4.07 \times 10^{-4}\hbar\omega_r$ . The corresponding critical particle difference yields  $\Delta N_c = 84.7$  and the small oscillation period  $\tau_{\text{SO}} = 65.4\omega_r^{-1}$ .

If such vortex orbits are centered in a positive coordinate, their periods coincide with the period of the orbit in the phase space, and the shape of the trajectory is ellipsoidal. In Fig. 11, such is the case of the vortex oscillation around  $Y_v^{(1)} = X_v^{(0)} \simeq 3.2l_r$ . On the other hand, there exists two vortices that move around  $x = y = 0$  with trajectories that encircle such a point and are always nearer the site with a lower number of particles. Such vortices pass from a  $(k)$  junction with  $Y_v^{(k)}$  ( $X_v^{(k)}$ ) to a  $(k+1)$  junction with  $X_v^{(k+1)}$  ( $Y_v^{(k+1)}$ ), when  $\varphi = \pi$  and have turning points in the same low-density paths at the turning points of  $\varphi(t)$  crossing to the neighborhood of the sites of lower number of particles. Such vortices display a “flower”-type orbit. As a consequence, the closed orbit of such vortices has twice the period of  $\varphi(t)$ . Moreover, since  $\Delta N(0) = 60$  is near the critical imbalance, the small oscillation approximation does not apply here, as it may be seen from the bottom panel of Fig. 11.

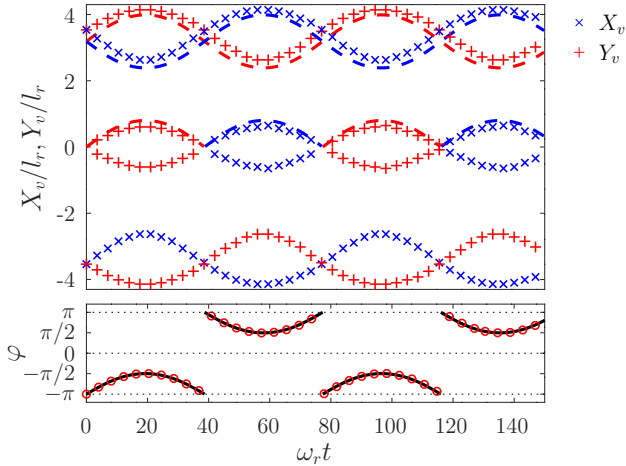


FIG. 11. Time evolution of the vortices coordinates (top panel) as depicted in Fig. 9 for  $\Omega/2\pi = 35\text{Hz}$ . The dashed red and blue lines correspond to Eqs (34) and (35), respectively. The corresponding phase difference  $\varphi(t)$  is depicted in the bottom panel. The initial conditions correspond to  $\varphi(0) = \pi$ ,  $N_0(0) = 2530$ , and  $N_1(0) = 2470$ . The dashed red and blue lines represent the predicted values from Eqs. (34) and (35), respectively, with  $l_y, l_x \in \{0; 1\}$ . In the bottom panel, the phase differences extracted from GP simulations and the MM model is depicted with red circles and a solid black line, respectively.

For  $\Re(K) > 0$  plasma modes are present and the central “flower”-type-vortex dynamics is absent. For low frequencies, the estimate of the stationary position yields a

value outside the lattice, and then, only part of the orbits may appear. In Fig. 12, we show such dynamics with a large rotation frequency  $\Omega/(2\pi) = 50\text{Hz}$  which corresponds to a hopping value  $\Re(K) = 1.68 \times 10^{-4}\hbar\omega_r$ , and a critical particle difference  $\Delta N_c = N_0 - N_1 = 54.4$ . In this case, two vortices move along each semiaxis around their corresponding stationary position, and the small oscillation approximation yields  $\tau_{\text{SO}} = 101.8\omega_r^{-1}$ , which is in good accordance with the period of the vortex orbits.

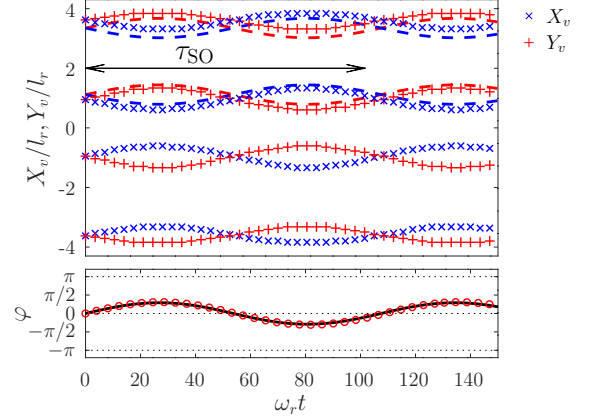


FIG. 12. Same as Fig. 11 for a rotation frequency  $\Omega/2\pi = 50\text{Hz}$ , and for the initial conditions  $\varphi(0) = 0$ ,  $N_0(0) = 2512.5$ , and  $N_1(0) = 2487.5$ . The time period  $\tau_{\text{SO}} = 101.8\omega_r^{-1}$  is indicated with an horizontal arrow. The indices  $l_x$  and  $l_y$  of the estimates from Eqs. (34) and (35), take the values  $\{0; 1\}$ .

## 2. Vortex dynamics for symmetric initial conditions with $\pm\pi/2$ - modes

In this section, we analyze the vortex dynamics for which the initial populations and phase differences verify  $n_k(0) = n_{k+2}(0)$  and  $\varphi_k(0) + \varphi_{k+1}(0) = \pi$ . Then, the vortex coordinates yield

$$Y_v^{(1)}(t) = \left( \frac{\varphi(t)}{\pi} + 2l_y + 1 \right) \frac{\pi\hbar}{mq_0\Omega}, \quad (36)$$

and

$$X_v^{(0)}(t) = \left( -\frac{\varphi(t)}{\pi} + 2l_x \right) \frac{\pi\hbar}{mq_0\Omega}. \quad (37)$$

Depending on the selected orbit, the central vortex can invert its charge during the dynamics. For low frequencies where  $\Im(K) \leq 0$ , only one vortex can appear along each semiaxis near the lattice border; hence we will focus on the case  $\Im(K) > 0$  given that a more interesting vortex dynamics emerges. In particular, we will consider the rotation frequency  $\Omega/2\pi = 45\text{Hz}$ , for which the imaginary part of the hopping parameter yields  $\Im(K) = 3.4138 \times 10^{-4}\hbar\omega_r$  and  $\Delta N_c = 77.48$ .

In Fig. 13 we show the vortex stationary configuration for the GP state  $\psi_{-1}(\mathbf{r})$  obtained by solving Eq. (1) that corresponds to the Hamiltonian minimum which is located at  $Z = 0$  and  $\varphi = -\pi/2$ , as can be verified from Eq. (5). Such vortex positions can be estimated using Eqs. (36) and (37) using  $\varphi(t) = -\pi/2$ , which yield  $Y_v^{(1)} = X_v^{(0)} \simeq 0.6l_r$  and  $3.1l_r$ , for  $l_y = 0$  and  $l_y = 1$ , respectively. We note that  $\psi_{-1}(\mathbf{r}) = \psi_{\text{MM}}(\mathbf{r})$  given by Eq. (3) with  $n_k = 0.25$ ,  $\phi_{-1} = \pi/2$ ,  $\phi_0 = 0$ ,  $\phi_1 = -\pi/2$ , and  $\phi_2 = \pi$ .

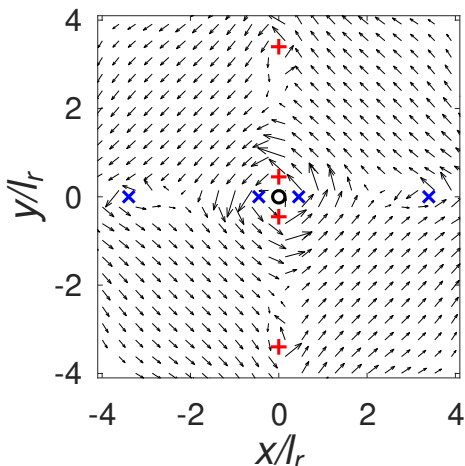


FIG. 13. Stationary vortex configuration in the  $(x, y)$ -plane, corresponding to the state  $\psi_{-1}(\mathbf{r})$  obtained from Eq. (1), for  $\Omega/2\pi = 45\text{Hz}$ . In connection to the TM model, such a state is related to the point  $\varphi = -\pi/2$  and  $Z = 0$  of the phase-space diagram. The vortices in the  $y$  and  $x$  axes are marked with red plus sign symbols and blue crosses, respectively. The central antivortex is shown as a black-hollow circle. The black arrows represent the velocity field.

Small phase-difference oscillations around  $-\pi/2$  may be viewed in the bottom panel of Fig. 14 with the corresponding vortex dynamics in top panel. There, the vortices oscillate but do not reach the origin of the  $x - y$  plane. Hence, the central antivortex located along the  $z$ -axis never change its charge. The small oscillation period obtained through Eq. (33) yields  $\tau_{\text{SO}} = 71.29\omega_r^{-1}$ , which is in good accordance with the numerical results. The selected orbit in the phase space diagram is depicted in the bottom panel of Fig. 7 which, as it can be seen, is entirely inside the dashed area in accordance with the permanence of the central antivortex.

Phase-difference oscillations with a larger amplitude can be viewed in Fig. 15, where in this case the central vortex changes its charge. Initially a central vortex is present, whereas when two vortices depart from the origin along the  $x$ -axis, depicted with the blue crosses in such a graph, a vortex-antivortex pair should be created in order to provide one of the vortices that depart as well as the central antivortex. An instant later, the other two vortices coming along the  $y$ -axis, which are indicated with red plus signs, provoke the annihilation of a

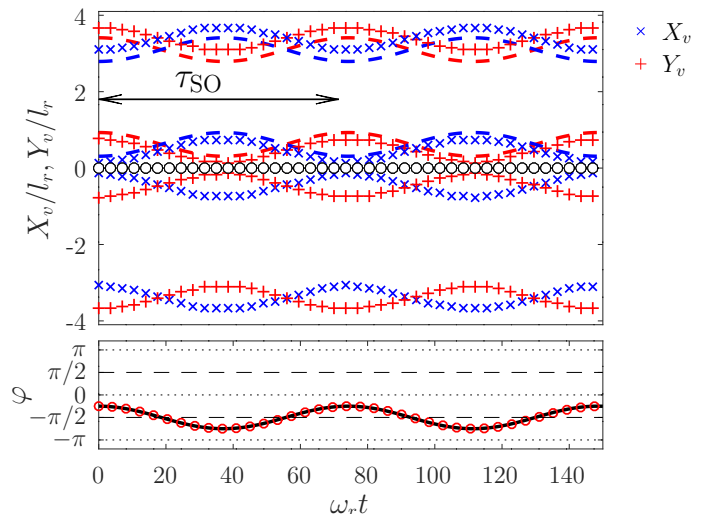


FIG. 14. Vortex coordinates as functions of time (top panel) extracted from the MM order parameter using the plaquette method, for  $\Omega/2\pi = 45\text{Hz}$ . The blue crosses and red plus signs of the positive coordinate values indicate  $X_v^{(0)}(t)$  and  $Y_v^{(1)}(t)$ , respectively, whereas the same symbols are utilized for the negative values which correspond to  $X_v^{(2)}(t)$  and  $Y_v^{(-1)}(t)$ . The black circles indicate the central antivortex. The dashed red and blue lines represent the predicted values from Eqs. (36) and (37), respectively. The initial conditions correspond to  $\varphi(0) = -\pi/4$  and  $Z = 0$ . The time period  $\tau_{\text{SO}} = 71.29\omega_r^{-1}$  is represented by an horizontal arrow. In the bottom panel, the phase difference is shown as a function of time, depicted with red circles and a solid black line, for the GP and MM model results, respectively.

vortex-antivortex pair and hence a single central vortex survives.

### C. Open orbits related to self-trapping regime

In the self-trapping regime, the imbalance oscillates around a nonvanishing value and the phase difference exhibits a monotonously increasing, or decreasing, behavior that is referred to as a running phase. The oscillation period for the Hamiltonian  $H_i$  can be approximated by [44]

$$\tau_{\text{st}} = \frac{Z_0 \pi \hbar}{2\mathcal{K}_i} \left[ 1 - \sqrt{1 - \frac{4}{\Lambda_i Z_0^2}} \right], \quad (38)$$

where  $Z_0$  is the imbalance value at the maximum of each corresponding open orbit.

An example of such types of evolutions is shown in Fig. 16, where in the bottom panel we depict the running phase difference for the Hamiltonian  $H_1$  and the related vortex dynamics is shown in the top panel. The rotation frequency corresponds to  $\Omega/2\pi = 45\text{ Hz}$ . From the bottom panel of Fig. 7 it can be seen that the maximum value of  $Z$  is achieved at  $\varphi = -\pi/2$ , which for

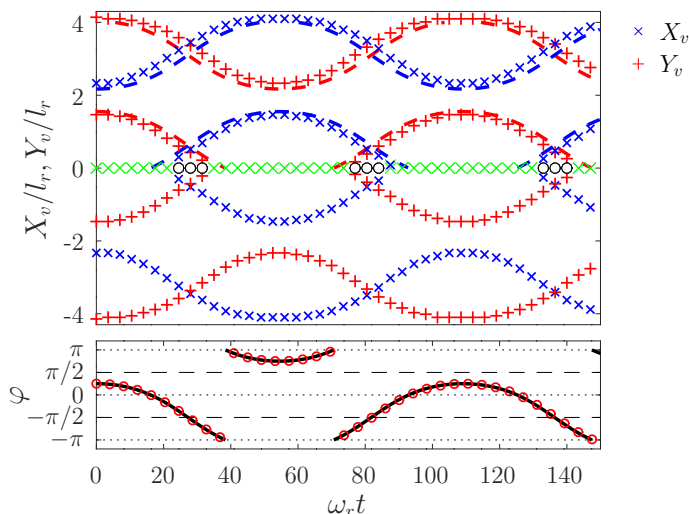


FIG. 15. Vortex coordinates as functions of time (top panel) extracted from the MM order parameter and depicted as in Fig. 14. The green crosses and the black circles indicate the central vortices and antivortices, respectively. The dashed red and blue lines represent the predicted values from Eqs. (36) and (37), respectively, with  $l_y = 0, 1$  and  $l_x = 0, 1$ . The initial conditions correspond to  $\varphi(0) = \pi/4$  and  $Z = 0$ , and the rotation frequency to  $\Omega/2\pi = 45\text{Hz}$ . In the bottom panel the phase difference  $\varphi(t)$  is depicted as in Fig. 14

the initial conditions considered in the present evolution, yields  $Z_0 \simeq 0.0253$ . Then, from Eq. (38) one obtains an estimate of the time period  $\tau_{\text{st}} = 24.4\omega_r$  which is in good agreement with the data of Fig. 16. Given that  $\dot{\varphi}(t)$  is always nonzero, the vortex trajectories do not possess turning points. If  $N_0 > N_1$  the vortices enter by the  $x$ -axis and depart from the system along the  $y$ -axis. Since the instant when vortices arrive at the  $z$ -axis do not coincide with the instant they leave it, there exist an inversion of the central vortex charge. The time such vortices spend in moving from the trap center up to the end of the lattice can be approximated by,

$$T_t = \frac{Lmq_0\Omega\tau_{\text{st}}}{\hbar 2\pi}, \quad (39)$$

where  $L = 4l_r$  denotes the largest absolute value of a vortex coordinate inside the lattice. Then, for the data of Fig. 16, we obtain  $T_t = 41.4\omega_r^{-1}$  (dashed arrow) in good agreement with the numerical result.

#### D. Comparison between the MM model and GP results for the position of the vortices

It may be seen from the bottom panels of the previous figures that in all cases the MM model accurately reproduces the GP phase difference, which constitutes the main ingredient for determining the vortex position. Nevertheless, small deviations in the vortex location can

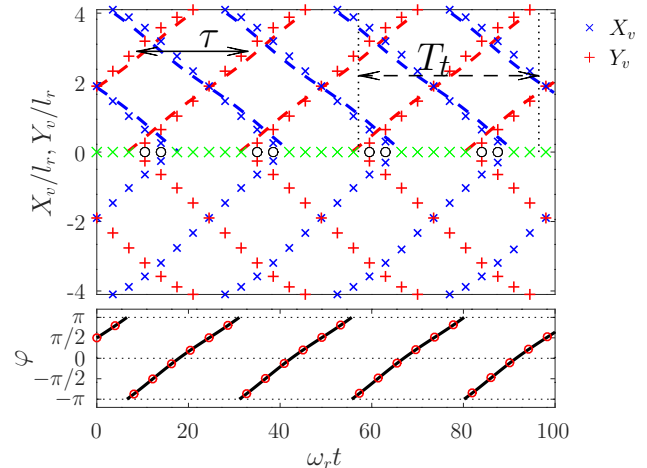


FIG. 16. Vortex positions and phase difference as functions of time are shown in the top and bottom panels respectively and depicted as in Fig. 10. The initial conditions are  $\varphi(0) = 0.5\pi$ ,  $N_0(0) = 2550$ , and  $N_1(0) = 2450$ . The horizontal arrows indicate the period  $\tau_{\text{st}} = 24.4\omega_r^{-1}$  and the traveling time  $T_t = 39.4\omega_r^{-1}$ . The rotation frequency corresponds to  $\Omega/2\pi = 45\text{Hz}$ .

occur due to density fluctuations of the time-dependent order parameter  $\psi_{\text{GP}}(\mathbf{r}, t)$ . Such small effects can be viewed in Fig. 17, where we have depicted the vortex coordinates extracted from  $\psi_{\text{GP}}(\mathbf{r}, t)$  using the plaquette method. The GP results are depicted in Fig. 17, with squares and triangles for the same conditions as in Fig. 12. Minor deviations between the squares and crosses or between the triangles and plus symbols can be observed except at the border of the condensate, where the density is very low and some larger fluctuations are present. During the evolution, short-living vortex-antivortex pairs can also be generated, and hence they slightly modify the position of the more stable vortices which we are interested in. For completeness, in Fig. 18 we also include a case where central vortices are present and one can observe a good accordance of the MM model with GP results, and both are well predicted by the estimate too.

## V. CONCLUSIONS

We have shown that the dynamics of vortices in a rotating lattice is determined by the phase differences between sites rather than by density gradients as it occurs in nonrotating systems. In particular, we demonstrate that different vortex dynamics can be engineered via the implementation of appropriate initial conditions on populations and phases in a rotating ring lattice. Such dynamics include open orbits associated with a running phase difference, in which case the vortices enter the lattice along one axis and exit along the other one without exhibiting turning points. The time of permanence of the vortex inside the lattice can be estimated by us-

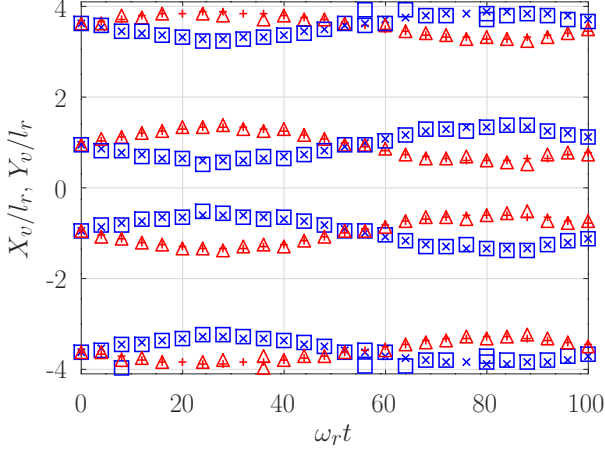


FIG. 17. Comparison between the GP and MM model vortex position as a function of time for the same conditions of Fig. 12. The blue squares (crosses) and red triangles (plus signs) indicate the coordinates of the vortices extracted from  $\psi_{\text{GP}}(\mathbf{r}, t)$  ( $\psi_{\text{MM}}(\mathbf{r}, t)$ ) order parameter along the  $x$  and  $y$  axes, respectively.

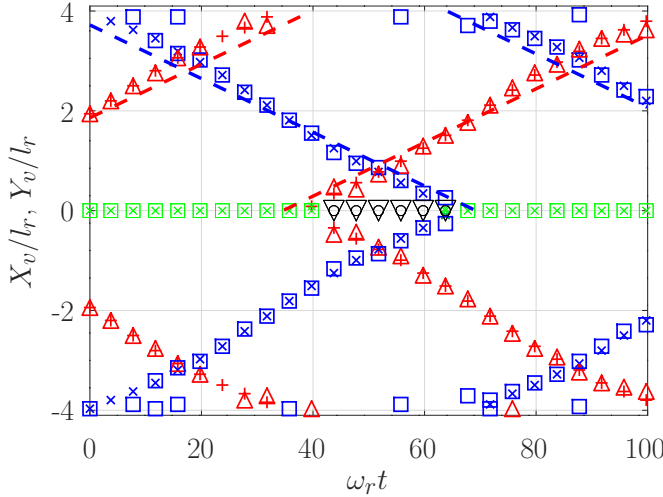


FIG. 18. Comparison between the GP and MM results as function of time, for  $N_0 = 2520$ ,  $N_1 = 2480$ ,  $\varphi(0) = 0$  and  $\Omega/2\pi = 30\text{Hz}$ . The red and blue symbols are the same of Fig. 17, whereas the green squares (crosses) and black triangles (circles) correspond to the central vortices and antivortices, respectively, extracted from  $\psi_{\text{GP}}(\mathbf{r}, t)$  ( $\psi_{\text{MM}}(\mathbf{r}, t)$ ) order parameter.

ing only the on-site interaction parameter in some cases, or evaluated via formulas developed for the self-trapping regime of a TM model. For particular initial phase differences, the dynamics involve the creation and annihilation of vortex-antivortex pairs at the center of the trap. The phase-space diagram of the associated Hamiltonian can be partitioned into regions where the central vortex or antivortex prevails, which hence allows us to predict when

such creation or annihilation processes occur. Closed orbits of vortices may be generated by choosing initial conditions near the minimum of the TM-model Hamiltonian. The related period turns out to be the same as that of the orbits of the model and can be easily evaluated in the case of small oscillations. The points on the  $x - y$  plane around which such oscillations occur approach the origin as the rotation frequency increases, and then more vortices oscillate around different points. In general, for open orbits, the velocity of the vortices inside the lattice decreases when the rotation frequency increases. We end by stressing that the accuracy of our approach is independent of the specific details of the trapping potential and on-site populations. Such an approach only requires that the system is formed by weakly linked spheroidal condensates with all their principal axes parallel to the rotation axis. In summary, we find that the present system constitutes a useful setting for studying different vortex processes, where both the orbits and the time periods can be predicted and applied in different settings.

### Appendix: Equations of motion and parameters of the multimode model

The equations of motion for  $n_k$  and  $\varphi_k$  can be obtained by inserting the MM order parameter of Eq. (3)

$$\begin{aligned} \hbar \frac{dn_k}{dt} &= 2|J| \left[ \sqrt{n_k n_{k+1}} \sin(\varphi_{k+1} + \theta_J) - \sqrt{n_k n_{k-1}} \sin(\varphi_k + \theta_J) \right] \\ &\quad - 2|F| \left[ \sqrt{n_k n_{k+1}} (n_k + n_{k+1}) \sin(\varphi_{k+1} + \theta_F) - \sqrt{n_k n_{k-1}} (n_k + n_{k-1}) \sin(\varphi_k + \theta_F) \right], \end{aligned} \quad (\text{A.1})$$

$$\begin{aligned} \hbar \frac{d\varphi_k}{dt} &= (n_{k-1} - n_k) N U_{\text{eff}} - \alpha (n_{k-1} - n_k) N U [N_s (n_{k-1} + n_k) - 2] \\ &\quad + |J| \left[ \left( \sqrt{\frac{n_k}{n_{k-1}}} - \sqrt{\frac{n_{k-1}}{n_k}} \right) \cos(\varphi_k + \theta_J) + \sqrt{\frac{n_{k-2}}{n_{k-1}}} \cos(\varphi_{k-1} + \theta_J) - \sqrt{\frac{n_{k+1}}{n_k}} \cos(\varphi_{k+1} + \theta_J) \right] \\ &\quad - |F| \left[ \left( n_k \sqrt{\frac{n_k}{n_{k-1}}} - n_{k-1} \sqrt{\frac{n_{k-1}}{n_k}} \right) \cos(\varphi_k + \theta_F) \right. \\ &\quad \left. + \left( 3 \sqrt{n_{k-2} n_{k-1}} + n_{k-2} \sqrt{\frac{n_{k-2}}{n_{k-1}}} \right) \cos(\varphi_{k-1} + \theta_F) - \left( 3 \sqrt{n_{k+1} n_k} + n_{k+1} \sqrt{\frac{n_{k+1}}{n_k}} \right) \cos(\varphi_{k+1} + \theta_F) \right], \end{aligned} \quad (\text{A.2})$$

where  $\varphi_k = \phi_k - \phi_{k-1}$ . The standard hopping parameter  $J$  and the interaction-driven one  $F$  are given by

$$J = - \int d^3r w_0^* (\hat{H}_0 - \Omega \hat{L}_z) w_1, \quad (\text{A.3})$$

$$F = -gN \int d^3r (w_0^*)^2 w_0 w_1. \quad (\text{A.4})$$

For  $\Omega \neq 0$ , such parameters  $J$  and  $F$  become complex numbers with phases  $\theta_J + \pi$  and  $\theta_F$ , respectively. On the other hand, as described in Ref. [45], the effective interaction parameter  $U_{\text{eff}}$  is obtained by calculating the on-site interaction energy parameter

$$U = g \int d^3r |w_0|^4, \quad (\text{A.5})$$

and evaluating the parameter  $\alpha$ , which takes into account the variation of the on-site interaction energy with the occupation number. Then, the effective interaction parameter yields  $U_{\text{eff}} = (1 - \alpha)U$ .

For our system setup in the nonrotating case, the standard hopping yields  $J = -6.60 \times 10^{-4} \hbar \omega_r$ , the interaction-driven hopping parameter  $F = 2.08 \times 10^{-3} \hbar \omega_r$ , the on-site interaction energy  $U = 3.16 \times 10^{-3} \hbar \omega_r$ , and the effective on-site interaction energy  $U_{\text{eff}} = 2.269 \times 10^{-3} \hbar \omega_r$ , being  $1 - \alpha \simeq 0.719$ . For more details, see Ref. [38].

For nonvanishing  $\Omega$  values, in the present work, the equations of motion will involve only a single hopping  $K$  defined by  $K = 2J + F = |K| e^{i\theta_K}$ . From the definitions of the hopping parameters, it is easy to demonstrate that

into Eq. (4), yielding [34]

the real and imaginary parts of the hopping  $K$  are related to the stationary states energies  $E_i$  by,

$$2\Re(K) = E_2 - E_0 \quad (\text{A.6})$$

and

$$2\Im(K) = E_1 - E_{-1}. \quad (\text{A.7})$$

With increasing values of  $\Omega$ , the absolute value of such hopping parameter monotonously decreases; whereas, given that the relative values of the energies change, both the real and imaginary parts of  $K$  alternate signs as functions of  $\Omega$ .

As a consequence of the geometry of the trap, when the system is subject to rotation the on-site localized states acquire a phase gradient which gives rise to a related, almost homogeneous, velocity field [34]. Such a particular phase profile determines the arguments of the hopping parameters, which turn out to be equal to a single phase  $\Theta \equiv \theta_K = \theta_J = \theta_F$  that obeys

$$\Theta = -\frac{m}{\hbar} \Omega r_{\text{cm}}^2 \sin(2\pi/N_s), \quad (\text{A.8})$$

where  $r_{\text{cm}}$  can be roughly approximated in terms of the intersite parameter.

Finally, with respect to the interaction energy parameters  $U$  and  $U_{\text{eff}}$ , they remain almost constant as functions of  $\Omega$  [34]. It is worthwhile to mention that, even though in the Thomas-Fermi (TF) approximation, the effective interaction energy parameter is reduced with respect to  $U$  by a factor of 7/10, 3/4, or 5/6, for either three, two, or one dimensions, respectively. Here, the

factor  $1 - \alpha \simeq 0.719$  has been obtained numerically, as

described in [34], which yields a slightly higher value than that corresponding to a TF 3D system.

- 
- [1] R. J. Donnelly, *Quantized Vortices in Helium II* (Cambridge University Press, Cambridge, 1991).
- [2] F. Dalfovo, S. Giorgini, L. P. Pitaevskii, and S. Stringari, *Rev. Mod. Phys.* **71**, 483 (1999).
- [3] A. L. Fetter, *Rev. Mod. Phys.* **81**, 647 (2009).
- [4] M. R. Matthews, B. P. Anderson, P. C. Haljan, D.S. Hall, C. E. Wieman, and E. A. Cornell, *Phys. Rev. Lett.* **83**, 2498 (1999).
- [5] B. P. Anderson, P. C. Haljan, C. E. Wieman, and E. A. Cornell, *Phys. Rev. Lett.* **85**, 2857 (2000).
- [6] K. W. Madison, F. Chevy, W. Wohlleben, and J. Dalibard, *Phys. Rev. Lett.* **84**, 806 (2000).
- [7] J. R. Abo-Shaeer, C. Raman, J. M. Vogels, and W. Ketterle, *Science* **292**, 476 (2001).
- [8] P. Engels, I. Coddington, P. C. Haljan, V. Schweikhard, and E. A. Cornell, *Phys. Rev. Lett.* **90**, 170405 (2003).
- [9] V. Bretin, S. Stock, Y. Seurin, and J. Dalibard, *Phys. Rev. Lett.* **92**, 050403 (2004).
- [10] S. Stock, B. Battelier, V. Bretin, Z. Hadzibabic, and J. Dalibard, *Laser Phys. Lett.* **2**, 275 (2005).
- [11] C. Ryu, M. F. Andersen, P. Cladé, V. Natarajan, K. Helmerson, and W. D. Phillips, *Phys. Rev. Lett.* **99**, 260401 (2007).
- [12] S. Eckel, J. G. Lee, F. Jendrzejewski, N. Murray, C. W. Clark, C. J. Lobb, W. D. Phillips, M. Edwards, and G. K. Campbell, *Nature (London)* **506**, 200 (2014).
- [13] K. E. Wilson, E. C. Samson, Z. L. Newman, and B. P. Anderson, *Phys. Rev. A* **106**, 033319 (2022).
- [14] S. Tung, V. Schweikhard, and E. A. Cornell, *Phys. Rev. Lett.* **97**, 240402 (2006).
- [15] R. A. Williams, S. Al-Assam, and C. J. Foot, *Phys. Rev. Lett.* **104**, 050404 (2010).
- [16] A. L. Fetter, B. Jackson, S. Stringari, *Phys. Rev. A* **71**, 013605 (2005).
- [17] J. K. Kim, A. L. Fetter, *Phys. Rev. A* **72**, 023619 (2005).
- [18] D. M. Jezek, P. Capuzzi, M. Guilleumas, and R. Mayol, *Phys. Rev. A* **78**, 053616 (2008).
- [19] D. E. Sheehy and L. Radzihovsky, *Phys. Rev. A* **70**, 063620 (2004).
- [20] H. M. Nilsen, G. Baym, and C. J. Pethick, *Proc. Natl. Acad. Sci. USA* **103**, 7978 (2006).
- [21] D. M. Jezek and H. M. Cataldo, *Phys. Rev. A* **77**, 043602 (2008).
- [22] A. J. Groszek, D. M. Paganin, K. Helmerson, and T. P. Simula, *Phys. Rev. A* **97**, 023617 (2018).
- [23] R. Navarro, R. Carretero-González, P. J. Torres, P. G. Kevrekidis, D. J. Frantzeskakis, M. W. Ray, E. Altuntas, and D. S. Hall, *Phys. Rev. Lett.* **110**, 225301 (2013).
- [24] T. Zhang, J. Schloss, A. Thomasen, L. J. O’Riordan, T. Busch, and A. White, *Phys. Rev. Fluids* **4**, 054701 (2019).
- [25] D. V. Freilich, D. M. Bianchi, A. M. Kaufman, T. K. Langin, and D. S. Hall, **329**, 1182 (2010).
- [26] T. W. Neely, E. C. Samson, A. S. Bradley, M. J. Davis, and B. P. Anderson, *Phys. Rev. Lett.* **104**, 160401 (2010).
- [27] T. W. Neely, A. S. Bradley, E. C. Samson, S. J. Rooney, E. M. Wright, K. J. H. Law, R. Carretero-González, P. G. Kevrekidis, M. J. Davis, and B. P. Anderson, *Phys. Rev. Lett.* **111**, 235301 (2013).
- [28] S. Serafini, M. Barbiero, M. Debortoli, S. Donadello, F. Larcher, F. Dalfovo, G. Lamporesi, and G. Ferrari, *Phys. Rev. Lett.* **115**, 170402 (2015).
- [29] A. M. Mateo and V. Delgado *Phys. Rev. Lett.* **97**, 180409 (2006).
- [30] J. A. Seman, E. A. L. Henn, M. Haque, R. F. Shiozaki, E. R. F. Ramos, M. Caracanhas, P. Castilho, C. Castelo Branco, P. E. S. Tavares, F. J. Poveda C., G. Roati, K. M. F. Magalhães, and V. S. Bagnato, *Phys. Rev. A* **82**, 033616 (2010).
- [31] M. Abad, M. Guilleumas, R. Mayol, F. Piazza, D. M. Jezek, and A. Smerzi, *EPL*, **109**, 40005 (2015).
- [32] Donadello, S. Serafini, M. Tylutki, L. P. Pitaevskii, F. Dalfovo, G. Lamporesi, and G. Ferrari, *Phys. Rev. Lett.* **113**, 065302 (2014).
- [33] D. M. Jezek, P. Capuzzi, H. M. Cataldo, *Phys. Rev. A* **93**, 023601 (2016).
- [34] M. Nigro, P. Capuzzi, and D. M. Jezek, *J. Phys. B: At. Mol. Opt. Phys.* **53**, 025301 (2020).
- [35] D. M. Jezek and P. Capuzzi, *Phys. Rev. A* **108**, 023310 (2023).
- [36] E. Poli, T. Bland, S. J. M. White, M. J. Mark, F. Ferlaino, S. Trabucco, and M. Mannarelli, *Phys. Rev. Lett.* **131**, 223401 (2023).
- [37] T. Bland, F. Ferlaino, M. Mannarelli, E. Poli, and S. Trabucco, *Few-Body Systems* **65**, 81 (2024).
- [38] M. Nigro, P. Capuzzi, H. M. Cataldo, and D. M. Jezek, *Phys. Rev. A* **97**, 013626 (2018).
- [39] H. M. Cataldo and D. M. Jezek, *Phys. Rev. A* **84**, 013602 (2011).
- [40] M. Albiez, R. Gati, J. Fölling, S. Hunsmann, M. Cristiani, and M. K. Oberthaler, *Phys. Rev. Lett.* **95**, 010402 (2005).
- [41] M. Nigro, P. Capuzzi, and D. M. Jezek, *Eur. Phys. J. D* **76**, 12 (2022).
- [42] C. J. Foster, P. B. Blakie, and M. J. Davis, *Phys. Rev. A* **81**, 023623 (2010).
- [43] A. Smerzi, S. Fantoni, S. Giovanazzi, and S. R. Shenoy, *Phys. Rev. Lett.* **79**, 4950 (1997).
- [44] M. Nigro, P. Capuzzi, H. M. Cataldo, and D. M. Jezek, *Eur. Phys. J. D* **71**, 297 (2017).
- [45] D. M. Jezek, P. Capuzzi, and H. M. Cataldo, *Phys. Rev. A* **87**, 053625 (2013).